Enhanced Superconductivity near the Pressure-Tuned Quantum Critical Point of Charge-Density-Wave Order in Cu1-δTe (δ = 0.016)

Kwang-Tak Kim , Yeahan Sur , Ingyu Choi , Zifan Wang , Sangjin Kim , Dilip Bhoi , Duck Young Kim * , Kee Hoon Kim *

Posted Date: 26 September 2025

doi: 10.20944/preprints202509.2167.v1

Keywords: superconductivity; charge density wave; pressure; quantum critical point; structural phase transition

 doi:10.20944/preprints202509.2167.v1

Article

Enhanced Superconductivity near the Pressure-Tuned Quantum Critical Point of Charge-Density-Wave Order in $Cu_{1-\delta}Te$ (δ = 0.016)

Kwang-Tak Kim [1], Yeahan Sur [1], Ingyu Choi [1], Zifan Wang [2], Sangjin Kim [1], Dilip Bhoi [1], Duck Young Kim [2,*] and Kee Hoon Kim [1,3,*]

[1] Center for Novel States of Complex Materials Research, Department of Physics and Astronomy, Seoul National University, Seoul 08826, Republic of Korea

[2] Center for High Pressure Science and Technology Advanced Research (HPSTAR), Shanghai 201203, China

[3] Institute of Applied Physics and Department of Physics and Astronomy, Seoul National University, Seoul 08826, Republic of Korea

* Correspondence: duckyoung.kim@hpstar.ac.cn (D.Y.K.); optopia@snu.ac.kr (K.H.K.)

Abstract

We have investigated the evolution of CDW states and structural phases in a Cu-deficient $Cu_{1-\delta}Te$ (δ=0.016) by employing high pressure experiments and first-principles calculations. Raman scattering results reveal that the vulcanite structure at ambient pressure starts to change into the Cu-deficient rickardite (*r*-CuTe) structure from 6.7 GPa, which then becomes fully stabilized above 8.3 GPa. Resistivity data show that T_{CDW1} (≈333 K) is systematically suppressed under high pressure, reaching zero at 5.9 GPa. In the pressure range of 5.2 - 8.2 GPa, a sharp resistivity drop due to superconductivity occurs at the onset temperature T_C= ~2.0-3.2 K. The maximum T_C =3.2 K achieved at 5.6 GPa is clearly higher than that of CuTe (2.3 K), suggesting importance of charge fluctuation in the vicinity of CDW suppression. At 7.5 GPa, another resistivity anomaly appears due to emergence of a second CDW (CDW2) ordering at T_{CDW2}=~176 K, which exhibits gradual increase to ~203 K with pressure increase up to 11.3 GPa. First-principles calculations on the Cu-deficient $Cu_{11}Te_{12}$ with the *r*-CuTe structure show that including on-site Coulomb repulsion is essential for incurring an unstable phonon mode relevant for stabilizing the CDW2 order. These results point out the important role of charge degree of freedoms in both optimizing the pressure-induced superconductivity and creating the competing CDW order in the Cu deficient CuTe system.

Keywords: superconductivity; charge density wave; pressure; quantum critical point; structural phase transition

1. Introduction

Low-dimensional materials exhibiting charge density wave (CDW) orders [1–9] have attracted significant attention due to their rich phase diagrams, including superconductivity (SC) [1,4], nematicity [5], and multiple density-wave orders [4–8]. Suppression of CDW by external parameters in those low-dimensional materials often leads to emergent novel quantum states, making them an ideal platform for exploring the interplay between the CDW and the competing quantum states. Archetypal examples include the case of transition-metal-dichalcogenides Pd_xTaSe_2, in which intercalating Pd ions between $TaSe_2$ layers suppresses the CDW and enhances SC near the CDW quantum critical point [1], and that of the kagome metals AV_3Sb_5 (A = K, Rb, Cs), at which the pressure-induced suppression of the CDW state results in two SC domes [8,9]

CuTe represents a prototypical example of exhibiting CDW order from the quasi-one-dimensional (Q1D) electronic structure. Angle-resolved photoemission spectroscopy has confirmed that the CDW transition appearing at T_{CDW1}=335 K at ambient pressure is driven by the Fermi surface

 doi:10.20944/preprints202509.2167.v1

nesting of Te 5p_x orbitals [10]. Under a high pressure condition [11,12], CuTe is known to exhibit a complex pressure-temperature phase diagram involving the interplay between the electronic phases of CDW and SC. As pressure increases, T_{CDW1} as evidenced by the resistivity r jump decreases linearly and reaches ~100 K near 6.5 GPa, above which this anomaly vanishes. From the pressure of ~6.7 GPa, another in-plane resistivity anomaly, a peak structure in dr/dT curve, appears at ~200 K, signaling stabilization of a second CDW phase (CDW2). With further increase of pressure up to 10 GPa, T_{CDW2} gets suppressed, being gradually lowered toward ~150 K; the resistivity anomaly at CDW2 finally vanishes beyond 10 GPa. Moreover, the superconductivity first emerges at a pressure of 4.8 GPa as a small resistivity drop at $T_C \approx 0.5$ K. T_C increases with further increase of pressure, showing a maximum at 2.3 K near 6.5 GPa, beyond which, T_C gradually decreases, consequently forming a dome-like phase diagram. Above 10 GPa, T_C becomes below 1 K, indicating significant suppression of SC with increasing pressure. At the pressures exceeding 20 GPa, CuTe undergoes a structural phase transition from the orthorhombic (*Pmmn*) to monoclinic (*Cm*) phase. In this new structural phase, superconductivity is stabilized with $T_C \approx 2.4$ K, persisting across the high-pressure range up to 49 GPa.

However, the nature of pressure-induced SC in CuTe, particularly its relationship with the CDW orders, remains elusive. As a possible mechanism for finding SC in the vicinity of CDW phases, two scenarios have been proposed [12]. First, a continuous suppression of CDW1 may increase charge fluctuation to enhance the pairing strength for superconductivity. However, this scenario is not applicable to the pristine CuTe as T_{CDW1} decreases to only 100 K at 6.5 GPa, thus mitigating the possibility of having quantum fluctuation of the CDW order parameters. Second, a mere competition between CDW and SC may induce the stabilization of SC at the expense of the competing CDW order. As common in a quasi-1D CDW system, the charge density modulation seems to involve significant lattice distortion so that the CDW transition with variation of temperature or pressure is clearly a first-order type. In particular, as a function of pressure, an abrupt first-order transition from CDW1 to CDW2 occurs at ~6.5-6.7 GPa so that SC is not a single competing phase of the CDW1 order. Indeed, SC stabilized at $4.8 \le P \le 10$ GPa also overlaps with the temperature and pressure windows where CDW2 phase stabilized (i.e.,7.5 GPa (T_{CDW2}= 204 K) £ P £ 10.1 GPa (T_{CDW2}= 173 K)). Therefore, the SC appears within the electronic structure created by the CDW2 phase rather than appearing directly at the expense of the CDW1 phase.

To address the puzzling question on the relationship between pressure-induced SC with the CDW order, we have investigated a $Cu_{1-\delta}Te$ (δ=0.016) single crystal using high-pressure studies of Raman spectroscopy, transport, and structural properties. Our study reveals that slight Cu deficiency significantly modifies the phase evolution, leading to $T_{CDW1} \approx 0$ K near 6 GPa and subsequent emergence of SC above 5.2 GPa with the maximum T_C ~ 3.2 K at 5.6 GPa. Furthermore, we find that a new structural phase, isostructural to the Cu-deficient rickardite CuTe (r-CuTe), appears above 6 GPa, thereby hosting the CDW2 order around 200 K. These findings suggest that understanding the role of Cu deficiency can be crucial for unraveling the intricate relationship between structural transitions, CDW orders, and superconductivity in the copper telluride system.

2. Methods

2.1. Single-Crystal Growth and Characterization

$Cu_{1-d}Te$ (d=0.016) single crystals were synthesized by a Te self-flux method. High-purity Cu powder (99.95%, Alfa aesar) and Te chunks (99.9999%, Alfa aesar) were mixed in a molar ratio of 1:2. The mixture was placed in an alumina crucible, which was then covered with another alumina crucible filled with quartz wool to enable filtration of the crystals from the Te flux after centrifugation. All the preparations were carried out in an Ar gas environment inside a glove box, of which oxygen and moisture concentrations were maintained below 1 ppm. The crucibles were subsequently sealed in evacuated quartz tubes. The ampules were heated to 660 °C and held at that temperature for 24 hours before being cooled down to 400 °C at a rate of 1 °C/h. Centrifugation was employed to separate the crystals from the Te flux, resulting in plate-like crystals with gold-colored surfaces. A typical size

 doi:10.20944/preprints202509.2167.v1

of the crystals was ~3×3×0.05 mm³. Room-temperature x-ray diffraction (XRD) measurements were performed using a high-resolution X-ray diffractometer (Empyrean™, PANalytical). To characterize the stoichiometry of the $Cu_{1-d}Te$ (d=0.016), wavelength dispersive x-ray spectroscopy was performed in a field emission electron probe microanalyzer (JEOL Ltd., A-8530F), installed at the National Center for Inter-university Research Facilities (NCIRF) at Seoul National University; Cu (99.8%) and Te (99.9999%) metals were used as standard specimens.

2.2. High-Pressure Transport and Raman Measurements

Longitudinal resistivity along the ***a***-axis and transverse Hall resistivity were measured by use of two lock-in amplifiers (SR830) and a standard Hall bar method. Temperature T and external magnetic fields H were controlled using a Physical Property Measurement System (PPMS™, Quantum Design). Pressure was applied using a diamond anvil cell attached with a pair of diamonds of a 300 μm culet size; sodium chloride (NaCl) powder was used as a pressure-transmitting medium and c-BN as the insulating layer. Raman measurements were performed using diamond anvil cells equipped with diamond anvils of a 300 μm culet size. Raman measurements at room temperature were conducted using a 532 nm laser beam with a power of 0.5 mW, and finely ground NaCl served as a pressure transmitting medium.

2.3. First-Principles Phonon Calculations

Phonon band structures for $Cu_{11}Te_{12}$ in the r-CuTe structure were calculated using the finite displacements method to obtain the dynamical matrix with Vienna ab initio simulation package (VASP) [14,15] and PHONOPY [16]. We used the generalized gradient approximation (GGA) of Perdew-Burke-Ernzerhof (PBE) [17] for the exchange-correlation functional with the cut-off energy of 600 eV. Monkhort-Pack k-point mesh with $0.03\cdot(2\pi/\text{Å})$ and $0.04\cdot(2\pi/\text{Å})$ mesh resolution was used for the structural optimization and phonon band structures calculation, respectively. For phonon calculations, we used the 2 × 2 × 2 supercell. We conducted the PBE +U calculations to account for the correlated d orbitals of Cu and $U_{\text{eff}} = U - J$ was chosen from 0 eV to 9 eV to investigate the Coulomb correlation effect on the structural instability. The effect of Van der Waals interaction was also considered using DFT-D3 method with zero damping (D3) [18].

3. Results

A. Crystallographic structure and basic physical properties of $Cu_{0.984}Te$

Figure 1a presents an XRD pattern of a $Cu_{0.984}Te$ single crystal. Only sharp (00l) diffraction peaks appear, indicating that the crystallographic ***c***-axis is perpendicular to the facet of the crystal. The measured (001) peaks match well with those of the vulcanite CuTe (v-CuTe, space group $Pmmn$). Independent XRD experiments on the grounded polycrystals have confirmed the v-CuTe structure (not shown here). Therefore, the $Cu_{0.984}Te$ crystal is isostructural to the v-CuTe structure, as illustrated in Figure 1b, at ambient pressure and at room temperature. In the v-CuTe structure, the Te chains are known to exist along the a-axis and each Cu atom forming a buckled Cu plane is bonded to the four Te atoms located below and above the Cu plane. As a result, the v-CuTe forms an orthorhombic $Pmmn$ structure with lattice constants a = 3.16 Å, b = 4.08 Å, and c = 6.93 Å. Wavelength-dispersive x-ray spectroscopy confirmed a Cu:Te ratio 0.984:1.00 (Figure S1, Table S1 in the supplemental information [19]), indicating slight Cu deficiency. We also measured the resistivity along the a-axis, ρ, in a $Cu_{0.984}Te$ single crystal, as shown in Figure 1c. Despite the slight Cu deficiency, we observe a clear resistivity upturn near 333 K, the feature similar to CuTe at its CDW state [10,11].

 doi:10.20944/preprints202509.2167.v1

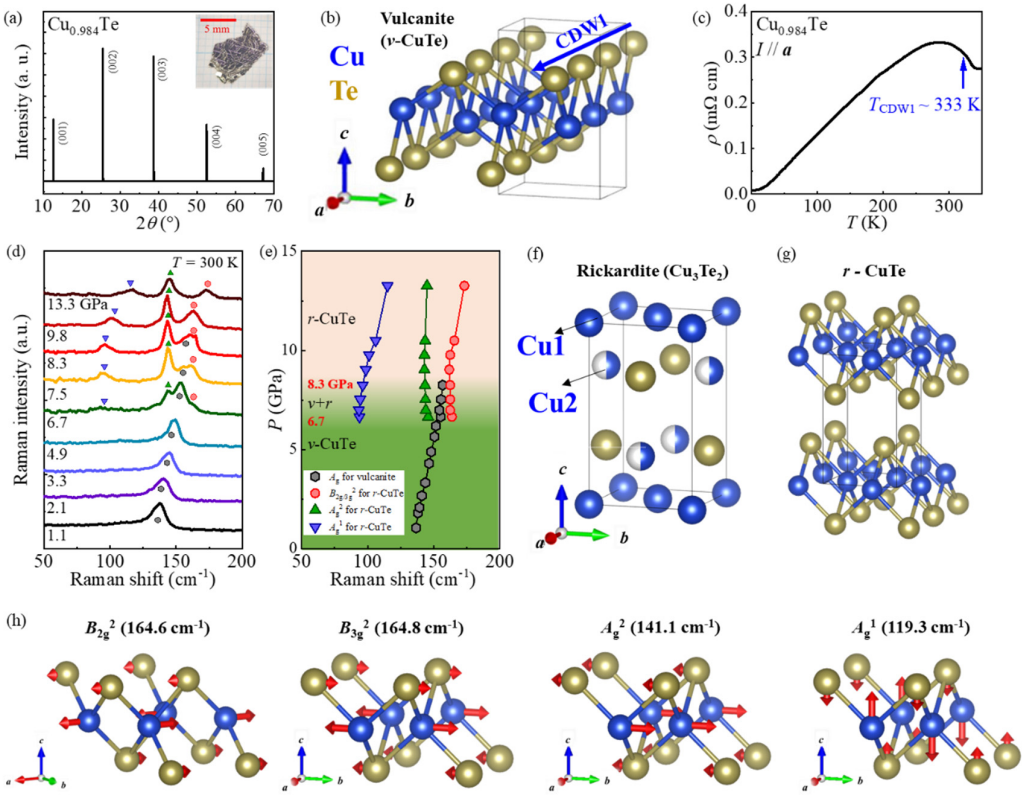

Figure 1. (a) The single-crystal X-ray diffraction pattern on the *ab*-plane of the single crystal $Cu_{0.984}Te$ at 300 K. The inset figure shows a picture of a typical $Cu_{0.984}Te$ single crystal by the flux methods. (b) The crystal structure of the vulcanite CuTe (*v*-CuTe). The blue arrow represents a quasi-one-dimensional Te chain direction exhibiting CDW (CDW1) order along the ***a***-axis. (c) The temperature dependence of the *a*-axis resistivity ρ of a $Cu_{0.984}Te$ single crystal at ambient pressure. The blue arrow indicates the CDW1 ordering temperature (T_{CDW1} = 333 K). (d) The raw data obtained from high-pressure Raman spectroscopy measurements at 300 K in the applied pressure range from 1.1 to 13.3 GPa. The assigned Raman phonon modes are indicated by the symbols. (e) The variation of Raman mode frequencies with pressure. The symbols appearing in (d) were used to represent each Raman mode. (f) The crystallographic structures of the rickardite (Cu_3Te_2), reproduced from [20]. (g) The crystallographic structures of the Cu-deficient rickardite *r*-CuTe, reproduced from [20]. (h) The vibration related to the representative Raman phonon modes in the *r*- CuTe structure, reproduced from Ref. [20].

B. Pressure-dependent evolution of Raman phonon modes

To monitor the structural evolution of $Cu_{0.984}Te$, we performed high-pressure Raman scattering using diamond anvil cells up to 13.3 GPa at room temperature as presented in Figure 1d. From the obtained scattering intensity, the pressure dependence of phonon mode frequencies was extracted as summarized in Figure 1e. Below 6.2 GPa, only one Raman mode was found at 136.6 cm^{-1}, which seems to be close to a theoretically predicted frequency of the A_{1g} mode (136.0 cm^{-1}) in the *v*-CuTe [11,21]. However, above 6.7 GPa, three new Raman modes, which do not correspond to the reported Raman modes of the *v*-CuTe [12,20], emerge at 163.8 cm^{-1}(**mode 1**), 145.8 cm^{-1}(**mode 2**), and 93.8 cm^{-1}(**mode 3**). Meanwhile, the original A_{1g} mode persists up to 8.3 GPa and disappears above the pressure. These spectral changes provide evidence that a new structural phase appearing at 6.7 GPa coexists with the low pressure *v*-CuTe up to 8.3 GPa and becomes solely stabilized above 8.3 GPa. Note that in the pristine CuTe, a pressure-induced structural transition has been reported to occur at 20 GPa from an orthorombic (*Pmmn*) to a monoclinic structure (*Cm*). However, no structural transition has been reported in a low-pressure regime around ~7 GPa [11,12].

 doi:10.20944/preprints202509.2167.v1

One might suspect that the newly appearing mode 2 and 3 at the high pressures may have originated from Te clusters [21] as they are indeed close to those of the *E* modes in pristine Te at ambient pressure (140.7 cm^{-1} and 92.2 cm^{-1}) [39,40]. However, if those modes were originated from the Te clusters, the A_1 mode of Te would have also been observed, since the intensity of the A_1 mode is known to be always stronger than those of the *E* modes and its frequency lies around ~120-100 cm^{-1} in a pressure regime below 15 GPa [39]. No signal that can be assigned as an A_1-mode of Te was detected around ~100-120 cm^{-1} in our experiments performed below 13 GPa. The minimum frequency of the A_1 mode of Te was previously found at ~100 cm^{-1} at a pressure of ~8 GPa [39]; its frequency at high pressures always remains higher than that of mode 3, leading to a conclusion that the mode 3 is not the A_1 mode of Te. Moreover, the Raman mode of Te has not been reported previously near the frequency region of ~164 cm^{-1} (that of mode 1) in a pressure window below 15 GPa, ruling out the possibility that the mode 1 can stem from the possible Te cluster. These observations suggest that the three modes emerging under the pressure above 6.7 GPa are unlikely to originate from possible Te clusters.

According to the previous density functional theory (DFT) calculations on CuTe [20], it was predicted that the Cu-deficient rickardite structure (*r*-CuTe) would have a lower formation energy than the *v*-CuTe. In this theoretical *r*-CuTe structure plotted in Figure 1g [20,22], the Cu2 sites of the rickardite Cu_3Te_2 (Figure 1f) located close to the four Te sites become completely vacant and remaining Cu sites form a flat Cu plane. Although the *r*-CuTe forms an orthorhombic structure (space group *Pmmn*) with lattice constants a = 3.845 Å, b = 3.847 Å, and c = 6.493 Å, it is indeed close to a tetragonal structure as it has similar in-plane lattice constants. However, this theoretical *r*-CuTe phase has not been found experimentally in the high-pressure region of CuTe [11,12].

We find in Figure 1d that three Raman modes appearing at the high pressures above 6.7 GPa match relatively well with those predicted for the *r*-CuTe in Ref. [20]; the phonon frequencies of mode 1 (163.8 cm^{-1}) and mode 2 (145.8 cm^{-1}) are close to those calculated for the B_{2g}^2/B_{3g}^2 (~164.7 cm-1) and the A_g^2 (141.1 cm^{-1}) modes, respectively. According to Figure 1e, the mode 3 frequency shows a drastic increase with pressure from 93.8 cm^{-1} at 6.7 GPa to 115.0 cm^{-1} at 13.3 GPa. As a result, the predicted A_g^1 mode frequency (~119.28 cm^{-1}) [20] is indeed close to the frequency of 115.0 cm^{-1} obtained at 13.3 GPa. As this A_g^1 mode involves the vibrational motion along the ***c***-axis, its frequency can be sensitive to the interlayer distance; consequently, the mode 3 indeed exhibits drastic hardening under pressure. Therefore, the mode 3 can be assigned as the A_g^1 mode predicted in the *r*-CuTe structure. On the other hand, we could not identify the additional phonon modes near the theoretically predicted B_{2g}^1/B_{3g}^1 mode (78.4 cm^{-1}) within our experimental resolution.

C. Temperature dependent resistivity under high pressures

To understand the evolution of electronic orders under external pressure, we have conducted temperature-dependent r measurements at pressures up to 12.9 GPa using a diamond anvil cell (Figure 2a,b). In the pressure regime starting from 0.5 GPa, we observe a clear r upturn around 318 K associated with the CDW1 ordering (a blue arrow). With further increase of pressure, the resistivity upturn is progressively weakened and its location is shifted to lower temperatures. Following a convention in the literature [23], we determine T_{CDW1} at each pressure as the peak temperature in the $d\ln(r)/d(1/T)$ curves (Figure 2c, blue arrows). As a result, T_{CDW1}, located at 333 K at ambient pressure, systematically decreases to 40 K at 5.9 GPa. At P above 6.0 GPa, the peak associated with the CDW1 in the $d\ln(r)/d(1/T)$ curves could not be identified.

 doi:10.20944/preprints202509.2167.v1

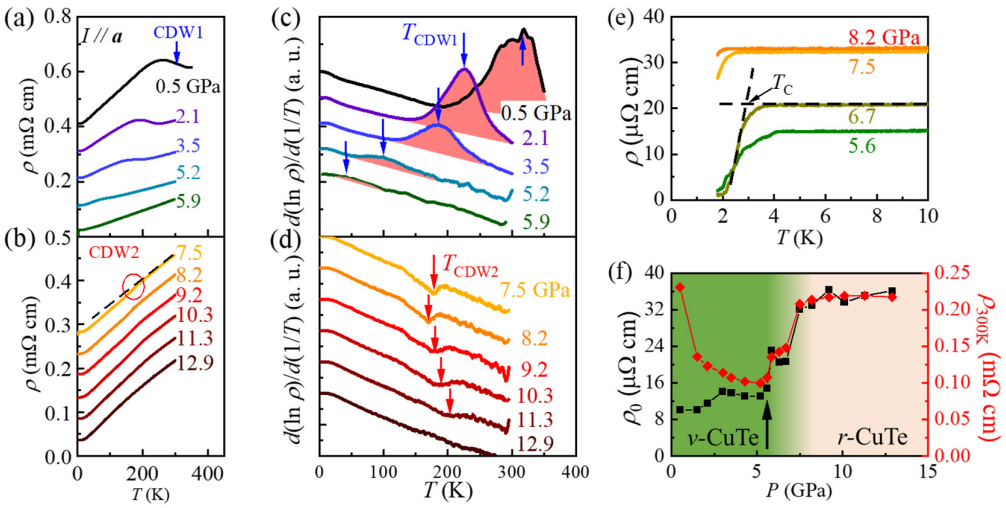

Figure 2. (a) Resistivity along the ***a***-axis (r) of a $Cu_{0.984}Te$ crystal at the pressure P below 5.9 GPa, exhibiting r increase due to the CDW1 (a blue arrow). The data is shifted down by a constant value (0.1 mΩ cm) for clarity. (b) r curves of $Cu_{0.984}Te$ at P above 5.9 GPa. A red circle highlights a region with small resistivity anomalies caused by the CDW2 phase, of which derivative is plotted in (d). The data is shifted down by a constant value (0.05 mΩ cm) for clarity. (c) The $d(\ln \rho)/d\ (1/T)$ vs. T plots at $P \leq 5.9$ GPa. The blue arrows indicate the peaks in each plot, representing T_{CDW1}. (d) The $d\ (\ln \rho)/d\ (1/T)$ plots at $P \geq 7.5$ GPa. The red arrows indicate the peaks due to stabilization of CDW2 phase in the new r- CuTe structure. Both data in (c) and (d) are shifted by a constant value for clarity. (e) r of $Cu_{0.984}Te$ under pressure at low temperatures exhibits a sharp drop due to the onset of the superconducting transition. (f) The pressure-dependent variation of residual resistivity (ρ_0) and resistivity at 300 K (ρ_{300K}). Both ρ_0 and ρ_{300K} exhibit sudden step-like increments (black arrows) at the pressures near 5.9 and 7.5 GPa.

With further increase of P, we find that another kink in the $d\ \ln(r)/d(1/T)$ curves emerges from 7.5 GPa and remains until ~11.3 GPa (red arrows in Figure 2d). Those kinks are linked to a weak resistivity drop, as illustrated in Figure 2b (red circles). Previous studies on the pristine CuTe have similarly found a small positive peak in the dr/dT curves [11]; it was assigned as the onset of the second CDW order (CDW2), based on the observation of the amplitudon mode from Raman scattering measurements [12]. As the peak feature in the dr/dT curves can appear as a dip in the $d\ln(r)/d(1/T)$ curve, we attribute the dip in the $d\ln(r)/d(1/T)$ curves to the onset of CDW2 order in $Cu_{0.984}Te$.

It is found in Figure 2d that the determined T_{CDW2} from the dip of the $d\ln(r)/d(1/T)$ curves exhibits non-monotonous changes with pressure; it decreases from 176 K at 7.5 GPa to 170 K at 8.2 GPa, and again increase to 203 K at 11.3 GPa. This behavior is in contrast to that found in a pristine CuTe where T_{CDW2}, determined from the peak in the dr/dT curve, continuously decreases with increase of P; $T_{CDW2} \approx 204$ K at 7.5 GPa decreases linearly down to $T_{CDW2} \approx 173$ K at 10.1 GPa [12]. Note that the dip feature in the $d\ln(r)/d(1/T)$ curve becomes progressively weakened with further P increase and finally disappears at 12.9 GPa. We also confirmed that the pressure-dependent evolutions of both T_{CDW1} and T_{CDW2} as revealed in the $d\ln(r)/d(1/T)$ curves of $Cu_{0.984}Te$ (Figure 2d) align well with those found in the dr/dT curves (Figure S2 in the Supplemental Information [19]).

At low temperatures, the drop of r, implying the onset of superconducting transition appears between 5.2 and 8.2 GPa (Figure 2e). The onset temperature of the superconducting transition (T_C) is determined by a crossing temperature from the two linear extrapolated lines (dashed lines in Figure 2e). As a result, T_C reaches a maximum of 3.2 K at 5.6 GPa and gradually decreases with increase of P. Note that this value is significantly higher than the maximum $T_C = 2.3$ K realized at $P \approx 5.7$ GPa in CuTe [12].

 doi:10.20944/preprints202509.2167.v1

As depicted in Figure 2f, we also find that both residual resistivity (r_0) and resistivity at 300 K (ρ_{300K}) remain small at $P \leq$~6 GPa (a black arrow) where the vulcanite structure is dominant. On the other hand, at $P \geq$~9 GPa where *r*-CuTe structure is dominant, both r_0 and ρ_{300K} reach the highest value. In an intermediate regime of 6.7 £ P £8.3 GPa, both r_0 and ρ_{300K} remain in the intermediate values and exhibit gradual increments. At this intermediate P regime, the Raman scattering results exhibit evidence of structural coexistence in $Cu_{0.984}Te$.

D. Structural phase transition and the emergence of CDW2

The emergence of CDW2 in $Cu_{0.984}Te$ and CuTe occurs in a different way. In the $Cu_{0.984}Te$, T_{CDW2} first appears at 176 K and at P = 7.5 GPa inside the pressure range where the *r*-CuTe structure coexists with *v*-CuTe structure (i.e., 6.7≤P ≤ 8.3 GPa) With the stabilization of the *r*- CuTe structure ($P \geq$ 8.3 GPa), T_{CDW2} decreases to 170 K, and increases again to 203 K as P increases to 11.3 GPa. In contrast, the pristine CuTe exhibits a sudden appearance of the CDW2 phase at 204 K at $P \geq$ 6.7 GPa in *v*-CuTe structure, and T_{CDW2} decreases monotonically with increasing pressure [11,12]. It was previously argued that the CDW2 phase in CuTe may stem from electronic correlation effects induced by four hole pockets originating from Te p_z orbitals, because there is no phonon softening or diverging electronic susceptibilities to support either electron-phonon coupling scenario or Fermi-surface nesting picture, respectively [12]. However, there is no concrete evidence in the theoretical calculations to support the scenario [12].

To better understand the origin of stabilizing the CDW2 phase in $Cu_{0.984}Te$, we have thus calculated phonon band structures of the *r*-CuTe with Cu deficiency, using the $Cu_{11}Te_{12}$ composition at 10 GPa (Figure 3). For this, the initial atomic positions of the r-CuTe structure, as provided in the supplementary data as a cif file, were used to have Cu deficiency in the Cu sites. Then, at 10 GPa, the atomic positions of *r*-CuTe structure with Cu deficiency has been relaxed. Since Coulomb interaction can affect the emergence of CDW2 as argued in CuTe [24], calculations were performed for the cases with or without Coulomb interaction (U). Without Coulomb interaction, there was no structural instability. However, the results reveal a negative phonon mode near the Z point when the Coulomb interaction U=9 eV is included. When U is systematically increase, it is found that the phonon mode softening was systematically increased at the Z point (See Figure S3 in the Supplemental Information [19]). Our independent calculations of the phonon band structure for the pristine CuTe (*v*-CuTe structure) for both with (U=9 eV) and without (U=0) Coulomb interaction did not result in any phonon anomaly (See Figure S4 in the supplemental information [19]). However, when the chemical potential of the CuTe electronic structure has been shifted toward the hole doped side, the effect of increasing U has also resulted in a similar negative phonon mode at a different momentum position (Figure S4). These results suggest that both Cu deficiency making hole-doping and increased Coulomb interactions should be important in the creating CDW2 phase in the high pressure region of $Cu_{0.984}Te$.

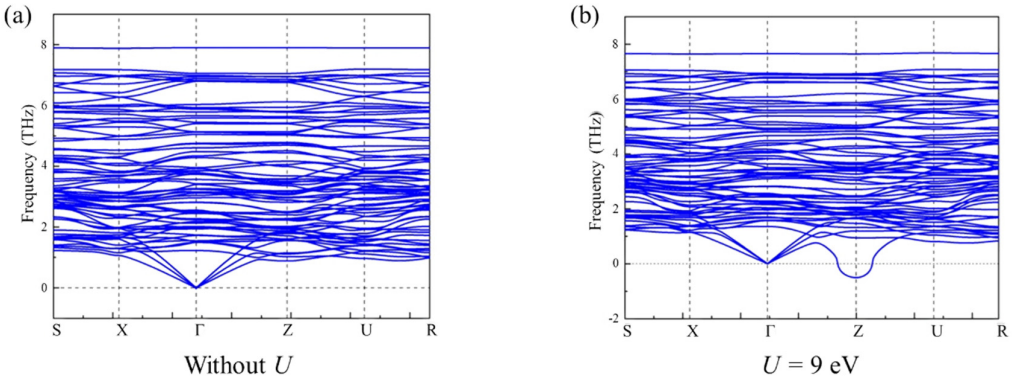

Figure 3. The result of phonon band calculation on the Cu deficient $Cu_{11}Te_{12}$ at 10 GPa, which is constrained to have the *r*- CuTe structure. ((a) without and (b) with coulomb interaction (U=9 eV).

 doi:10.20944/preprints202509.2167.v1

E. Magnetotransport measurements under high pressure

To monitor evolution of electronic structure with pressure, we conducted magnetoresistance (MR) and Hall effects measurements at various pressures. Figure 4a shows the MR curves, $D\rho(H)/\rho(0) \equiv (\rho(H) - \rho(0))/\rho(0)$ at 10 K, and at $P \geq 1.5$ GPa. For $1.5 \leq P \leq 5.6$ GPa where CDW1 is stabilized, the MR at 10 K is particularly large, reaching 10- 110% at 9 T. Moreover, at this P regime, MR shows a crossover from H-quadratic at $\mu_0 H \leq 2$ T (dashed blue line) to linear dependence above $\mu_0 H \geq \sim 3$ T (dashed red guide lines). As P increases from 1.5 to 5.6 GPa, MR at 9 T decreases from 110 to 10%, accompanied by similar decreases of the linear slope (red dashed lines). Therefore, the large MR and the linear slope proportional to the MR value should be attributed to the characteristic features of the CDW1 state.

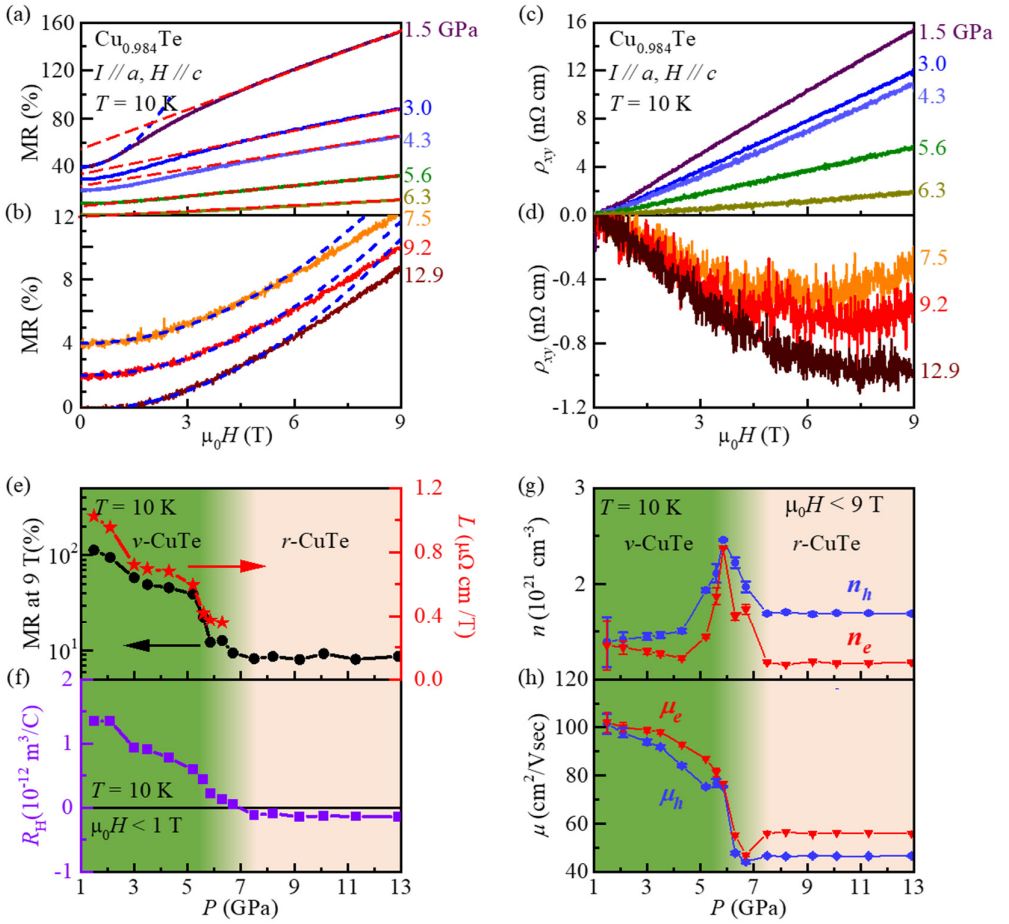

Figure 4. (a) Magneto-resistance (MR) data for $P \leq 6.3$ GPa at 10 K. The red dashed lines represent the linear MR region observed above 3 T, which is coined to emerge within the pressure range of having the CDW1 order as a ground state. The blue dashed line represents the quadratic MR region observed below 2 T in MR data for P = 1.5 GPa. The data is shifted by a constant (10%) for clarity. (b) The MR data for $P \geq 7.5$ GPa at 10 K. The blue dashed lines represent the quadratic MR region observed below 6 T The data is shifted by a constant (2%) for clarity. (c) Hall resistivity data r_{xy} at 10K for $P \leq 6.3$ GPa. (d) r_{xy} at 10K for $P \geq 7.5$ GPa. (e) The MR value at 9 T (black circles) and the linear slope L ($\rho(H) = \rho_0 + \mu_0 L|H|$) extracted from $\rho(H)$ curve at $\mu_0 H \geq \sim 3$ T (red stars). (f) Pressure dependence of the Hall coefficient (R_H) at 10K and $\mu_0 H < \sim 1$ T. (g) Pressure-dependence of hole and electron carrier densities (n_h and n_e) and (h) their mobilities (μ_h and μ_e) as obtained by the analyses of r_{xy} by a two-band model.

For $P > 6.3$ GPa and at 10 K (Figure 4b) where the CDW2 state in the r-CuTe structure is dominantly stabilized, the MR values become less than 10% at $\mu_0 H$=9 T; they are clearly smaller than

 doi:10.20944/preprints202509.2167.v1

those in the lower pressure regime. Moreover, the field-dependence of MR, being proportional to $\rho(H)$, exhibits mostly quadratic behavior, i.e., $\rho(H) \propto H^{\beta}$ with b »2 at m_0H £ ~6 T (dashed blue lines). Detailed analyses of the $d\rho(H)/dm_0H$ curves (Figure S5 in the Supplemental Information [19]) are also consistent with such quadratic H dependence at the region where the CDW2 state in the *r*-CuTe structure is realized.

Numerous materials with CDW order have often exhibited large linear MR below their T_{CDW}'s [25]. In those cases, the CDW transition can create small electron or hole pockets with sharp curvature, called "sharp corners" in the momentum space. Electrons traveling along these sharply curved trajectories experience abrupt momentum changes, thus strongly influencing the resistivity values. Under magnetic fields, the electrons experience the Lorentz force, causing them to follow the trajectories with a cyclotron frequency proportional to H. This means that as H increases, the electrons pass through the trajectory more quickly and thus increases the probability of interaction with the sharp corners. As a result, the number of electrons interacting with such sharp corners can increase linearly with H, explaining how the CDW state can lead to the linear MR.

Based on the hypothesis that the linear MR in $Cu_{0.984}Te$ (Figure 4a) is also caused by the sharp corners in the momentum space as formed inside the CDW1 state [10], we try to extract the slope L predicted by the formula of $\rho(H) = \rho_0 + m_0L|H|$. Figure 4e shows the resultant L extracted from the MR data (Figure 4a, $m_0H \geq 3$ T) at each pressure; the MR value at m_0H = 9 T at 10 K is also plotted together. It is found that as P increases, both L and MR at 9 T systematically decrease up to 5.9 GPa, at which the CDW1 state is nearly suppressed to become T_{CDW1}=40 K (not shown). At P=6.3 GPa, the MR exhibits only linear H-dependence down to ~2 K. With further increase of $P \geq 6.3$ GPa (Figure 4b), linear MR behavior disappears (thus L vanishes) and quadratic H-dependence becomes dominant in the $\rho(H)$ curves as well shown in the three representative curves from 7.5 to 12.9 GPa. Moreover, the MR values at 9 T become saturated at ~10%. These results suggest that the reconstructed electronic structure formed by the CDW1 state produces sharp corners in the momentum space to result in the large linear MR. Moreover, upon pressure being increased to enter the CDW2 state, the sharp corners may have almost disappeared.

Figure 4c,d show the Hall resistivity r_{xy} at 10 K measured at various P £ 6.3 and ³ 7.5 GPa, respectively; the evolution of the Hall coefficient R_H extracted at the curves below 1 T is also summarized in Figure 4f. At P £ ~5.9 GPa where the CDW1 order is stabilized, the positive R_H values (Figure 4f) systematically decrease with increase of P, indicating that effective carrier density increases with the gradual decrease of the electronic gap inside the CDW1 state. However, even at P ≥ 6.3 GPa where the CDW1 state is no longer stabilized at a finite temperature, R_H keeps decreasing to becomes negative at P = 7.5 GPa, from which nearly the same negative value is maintained up to P=12.9 GPa. In addition, followed by the sign change of R_H near 7.5 GPa, ρ_{xy} starts to exhibit nonlinear H-dependence in the pressure region of ~7.5 £ P £ 12.9 GPa (Figure 4d). As R_H values (also ρ_{xy} behaviors) are similar at 7.5 £ P £ 12.9 GPa, irrespective of the phase boundaries of CDW2 (7.5 £ P £ 11.3 GPa), it is expected that the *r*-CuTe structure, not the CDW2 state, mainly determines the electronic structures.

To analyze the H-dependence of r_{xy} under pressure, we used a two-band model with one hole and one electron bands [26,27]:

$$\rho_{xy} = \frac{B}{e}\frac{(n_h\mu_h{}^2 - n_e\mu_e{}^2) + (n_h - n_e)\mu_h{}^2\mu_e{}^2B^2}{(n_h\mu_h + n_e\mu_e)^2 + (n_h - n_e)^2\mu_h{}^2\mu_e{}^2B^2}$$

Here, n_h (n_e) represents the hole (electron) density, μ_h (μ_e) is the hole (electron) mobility, e is one electron charge, and B is the magnetic induction. This model was applied to fit the r_{xy} curve at each pressure (see Figure S6 in the Supplemental Information [19]) and the parameters n_h, n_e, μ_h, and μ_e obtained from the fit are summarized in Figure 4g,h. It is found that at ~4.3£ P£ 7.5 GPa, both n_h and n_e are sharply increased, forming maximum values at the critical pressure of ~ 5.9 GPa, at which a quantum critical point of the CDW1 state is expected to exist. Simultaneously, both μ_h and μ_e exhibit nearly two-fold decrease from P ≈ 3.5 to 6.7 GPa and a slight increase at 7.5 GPa, thus forming a minimum at 6.7 GPa. At P³ ~7.5 GPa, μ_h and μ_e remain nearly constant. These observations suggest

 doi:10.20944/preprints202509.2167.v1

that a continuous gap closing of the CDW1 state by P increase up to ~5.9 GPa and associated critical fluctuation of charge amplitude might cause the increase of carrier densities and the decrease of carrier mobilities [28]. This aligns with the diminishing linear MR as P approaches ~5.9 GPa, showing that the suppression of the CDW1 order is significantly affecting the transport properties.

When a single CDW state is collapsed within the same crystal structure, thereby closing the CDW gap, it is common to observe the increase of the carrier densities outside the CDW state [29]. However, our results indicate that near the structure coexistence region of the v- and r- CuTe (~6.7 £ P £ 8.3 GPa), the n_h and n_e show abrupt decreases from 6.3 GPa while μ_h and μ_e increase slightly. This suggests that albeit having the gap closing of the CDW1 state, the creation of different structural phases may have resulted in the abrupt reduction of carrier densities. Besides, possible extra-scattering of carriers at the structural domain walls, if any, may be negligible as compared with the effect of critical fluctuation of the CDW1 order (both CDW amplitude and phase). Furthermore, at P ≥ 7.5 GPa where the CDW2 state is stabilized, decreasing behavior of n_h and n_e values are saturated to remain nearly same, indicating that the electronic structure, as influenced by the CDW2 state in the r-CuTe phase, is less sensitive to the pressure-variation.

4. Discussion

Figure 5a summarizes the pressure-temperature phase diagram of $Cu_{0.984}Te$, highlighting distinct regions of structural and electronic phases. Raman spectroscopy, resistivity, and magnetotransport data are used to construct the structural and electronic phase boundaries. The ambient v-CuTe structure is stabilized below 6.7 GPa within which the CDW1 order emerges at low temperatures below T_{CDW1}. As described in the Results, the r-CuTe structure coexists with the v-CuTe structure between 6.7 and 8.3 GPa. Above 8.3 GPa, the system fully transforms into the r-CuTe phase. The CDW2 emerges at ~176 K at P = 7.5 GPa and T_{CDW2} is gradually enhanced up to 203 K with pressure increase up to 11.3 GPa. However, above 11.3 GPa, the experimental signature of the CDW2 state (i.e., dip in the $d\ln(r)/d(1/T)$ curves in Figure 2d) disappears.

 doi:10.20944/preprints202509.2167.v1

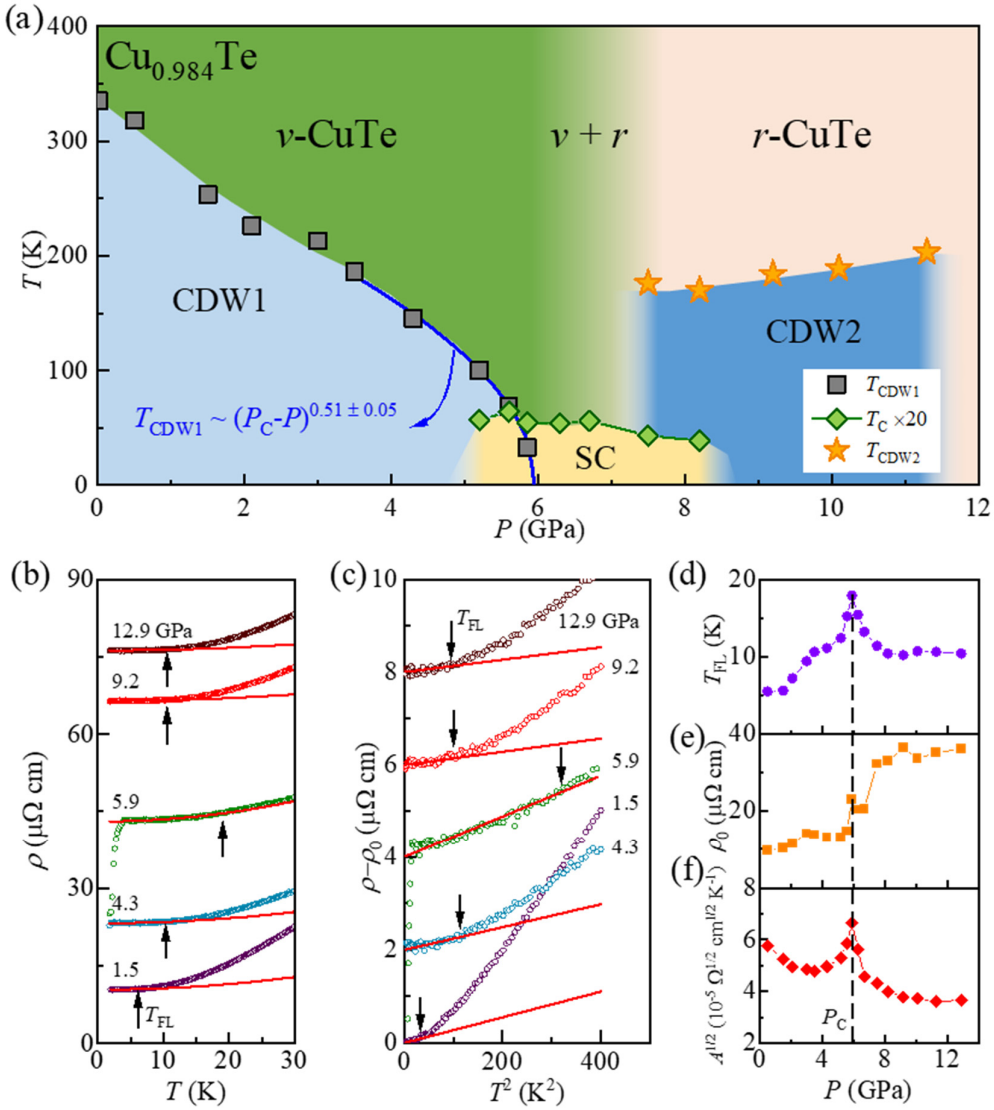

Figure 5. (a) The temperature-pressure (T-P) phase diagram of $Cu_{1-\delta}Te$ (δ=0.016). The blue dashed line indicates the suppression of CDW1 order. The blue solid line represents the power-law fitting ($T_{CDW1} \sim (P_C\text{-}P)^{0.51 \pm 0.05}$ with P_C = 5.98 ± 0.05 GPa). In the region of green colors and CDW1 state, the v- CuTe structural phase is stabilized while the pink region and the CDW2 region, a new structural phase of r- CuTe is stabilized. In the intermediate pressure range pf ~6.7≤P≤ ~8.3 GPa, the two structural phases of the v- CuTe and r-CuTe are coexistent. (b) The r curves measured under pressures and low temperatures. The results obtained at the temperatures above the superconducting states are fitted by a quadratic power law $\rho = \rho_0 + AT^2$ (red solid lines). (c) The plots of ($\rho_{ab} - \rho_0$) vs. T^2 for various pressures. The red lines are linear guidelines. The black arrows in (b) and (c) indicate the effective Fermi liquid temperature T_{FL}. (d) The pressure dependence of T_{FL}. (e) and (f) indicate the pressure-dependent evolution of the fitting parameters ρ_0 and $A^{1/2}$ obtained from the best fit to $\rho = \rho_0 + AT^2$ curves below T_{FL}. The black dashed indicates the critical pressure P_C obtained from the power law fitting described in Figure 5a.

We should note that the structural/electronic phase evolution of $Cu_{0.984}Te$ differs significantly from that of the pristine CuTe [12] in several aspects. Firstly, CDW1 in $Cu_{0.984}Te$ is continuously suppressed with pressure to reach T_{CDW1}=40 K at 5.9 GPa and the signals related to the CDW1 cannot be found in the transport data above 6.0 GPa. In contrast, the CDW1 sate of the pristine CuTe persists up to 6.5 GPa and exhibits T_{CDW1} ~100 K near 6.5 GPa. Secondly, in the $Cu_{0.984}Te$, we observe a clear structural phase transition into the r-CuTe structure and the emergence of the CDW2 state within the

 doi:10.20944/preprints202509.2167.v1

r-CuTe structure. This new structure was absent in the pristine CuTe while the CDW2 state in CuTe has been found at 7.5£ *P*£ 10.3 GPa. This indicates that the high-pressure structure is not an essential part of inducing the CDW2 instability. Thirdly, T_{CDW2} in $Cu_{0.984}Te$ increases with pressure from 170 K at 8.2 GPa to 203 K at 11.3 GPa. However, T_{CDW2} in CuTe decreased with pressure increase; it is found at 204 K at 7.5 GPa and 173 K at 10.3 GPa. Therefore, the slight deficiency of Cu significantly affects the both electronic and structural phase boundaries.

The CDW1 state in $Cu_{0.984}Te$ shows decrease of T_{CDW1} with pressure increase. Indeed, we found that T_{CDW1} decreases rapidly in the low- *P* regime (*P* £ 3.5 GPa) (Figure 5a). On the other hand, above 3.5 GPa, where *P* approaches toward 6 GPa, T_{CDW1} follows a power-law behavior with $T_{CDW1} \propto \left(\frac{P_C - P}{P_C}\right)^{0.51 \pm 0.05}$ with $P_C \sim 5.98 \pm 0.05$ GPa. This power-law behavior with the exponent 0.5 is a typical behavior expected in a mean-field type phase transition [30]. This characteristic mean field behavior has been also found in several materials near the quantum critical point (QCP) [28,31–34], including $NbSe_3$ [31,32] and β-vanadium bronze [31,33], which belong to the Q1D materials exhibiting a CDW formation and a charge ordering, respectively. This emergence of power-law behavior in $Cu_{0.984}Te$ thus strongly suggests that it may undergo a pressure-induced quantum phase transition of the CDW state, and the CDW fluctuation near P_C plays a role in enhancing T_C.

On the other hand, the continuous evolution of T_{CDW1} with pressure, following power-law behavior near P_C is distinctly different from that of the pristine CuTe, in which T_{CDW1} decreases almost linearly to 100 K at 6.5 GPa and disappears suddenly in a first-order manner above 6.5 GPa [12]. The different pressure responses suggest that Cu deficiency may allow the continuous decrease of the electronic CDW1 order parameter (i.e., CDW amplitude) to form the pressure-induced CDW-QCP at 5.98 GPa. For this, the structural transition expected in the CDW instability is decoupled so that the associated anomaly in the Te chain occurs at a higher pressure regime (>6.3 GPa). Note that this behavior is clearly different from that observed in a typical 1D-CDW system, in which a first-order CDW transition often occurs together due to the associated large entropy change involved in the lattice modulation.

To investigate the possible effect of charge fluctuations near P_C on transport phenomena, we have studied the pressure-dependent evolution of the Fermi-liquid behavior at low temperatures above T_C (Figure 5b,c). According to Fermi-liquid theory, ρ exhibits a quadratic *T*-dependence of $\rho = \rho_0 + AT^2$, where ρ_0 is a residual resistivity and *A* is the coefficient of the quadratic term [35]. In our data for $P \leq 1.5$ GPa, the quadratic power-law successfully describes the ρ (*T*) behavior below ~ 5 K, defined as an effective Fermi-liquid temperature T_{FL}. Above T_{FL}, the results deviate from the Fermi-liquid behavior. This indicats that the electron-electron scattering causing the Fermi liquid behavior is dominant in the transport behavior at ambient and low pressure region ($P \leq 1.5$ GPa) below T_{FL}, while the other factors, such as electron-phonon coupling, become more important above T_{FL}.

It is found that the quadratic *T*-dependence persists across all the *P* ranges studied. Figure 5c shows the ($\rho_{ab} - \rho_0$) vs. T^2 plots at various pressures, indicating that ($\rho_{ab} - \rho_0$) is linear with T^2 below T_{FL}. As *P* increases, T_{FL} rises from 5.6 K at 1.5 GPa to 17.9 K at 5.9 GPa, suggesting an enhancement of the effective Fermi-liquid energy scale near P_C. However, after reaching a maximum at $P \sim P_C$, T_{FL} drops to ~10 K at 8.2 GPa and remains nearly constant up to 12.9 GPa. (Figure 5d). This behavior can be interpreted as a modification of the Fermi surface by *P*. A larger Fermi surface implies that electrons can maintain a well-defined quasiparticle distribution over a wider *T* range, thereby possibly elevating T_{FL}. Since the suppression of CDW1 often leads to an enlarged Fermi surface, the sharply enhanced T_{FL} near P_C should be attributed to the increased Fermi surface area. The observed *P*-dependent increase of the carrier densities up to 5.9 GPa (Figure 4g) is also consistent with this picture. However, sharp decreases of both carrier density and T_{FL} above 5.9 GPa, and their saturated behavior above 8.2 GPa indicates that the full stabilization of the *r*-CuTe structure above *P* = 8.2 GPa and its resultant electronic band structure limits the increase of carrier density and Fermi surface.

In the Fermi liquid state, it is known that the Kadowaki-Woods relation, $A = \alpha_{KW} \gamma_0^2$ [36], where α_{KW} is the Kadowaki-Woods ratio and γ_0 is the Sommerfeld coefficient, is satisfied, resulting in the relation that $A^{1/2} \propto \gamma_0$. Moreover, γ_0 can be expressed as $\gamma_0 = \frac{1}{3}\pi^2 k_B^2 (1 + \lambda_{ee} + \lambda_{ep}) N(\varepsilon_F)$[37], where k_B

 doi:10.20944/preprints202509.2167.v1

is the Boltzmann constant, $\lambda_{ee}(\lambda_{ep})$ is the electron-electron (electron-phonon) coupling constant, and $N(\varepsilon_F)$ is the electronic density of states at Fermi level. Based on the experimental data summarized in Figure 5c, we have extracted the pressure-dependent evolution of $A^{1/2}$ (Figure 5f). Below 3.0 GPa, $A^{1/2}$ decreases from 5.75×10^{-5} $\Omega^{1/2}$cm$^{1/2}$K^{-1} at 0.5 GPa to 4.79×10^{-5} $\Omega^{1/2}$cm$^{1/2}$K^{-1} at 3.5 GPa. However, in the range 3.5 - 6.7 GPa near P_C, $A^{1/2}$ exhibits a sharp peak reaching a maximum of 6.65×10^{-5} $\Omega^{1/2}$cm$^{1/2}$K^{-1} at 5.9 GPa. With increasing pressure, $A^{1/2}$ gradually decreases again up to 12.9 GPa.

According to the Kadowaki-Woods relation, the evolution of $A^{1/2}$ provides insights into changes in λ_{ee}, λ_{ep}, and $N(\varepsilon_F)$. Since the new structural phase in $Cu_{0.984}Te$ appears above 6.7 GPa, λ_{ep} likely does not change significantly near P_C [35]. Hence, the increased $A^{1/2}$ near P_C seems to arise from the enhancement in $N(\varepsilon_F)$ or λ_{ee}. As the effective Fermi surface area is expected to increase upon closing the CDW1 gap, increasing trend of the T_{FL} and the carrier density across P_C can be reasonably understood. This may be accompanied by gradual decrease of $N(\varepsilon_F)$ as the pressure evolution of electronic structure can result in decrease of the effective mass. In our experimental results, $A^{1/2}$ indeed exhibits gradually decreases in both low and high pressure regions except near P_C, indicating that the gradual decrease can be explained by the overall decrease of $N(\varepsilon_F)$ with pressure. However, to explain the sharp increase of $A^{1/2}$ near P_C, where the critical fluctuations of the CDW order parameter is expected, we conjecture that the λ_{ee} increase plays an important role. A similar sharp enhancement of $A^{1/2}$ near P_C has been also observed recently in other systems with a CDW-QCP, such as 2*H*-$Pd_{0.05}TaSe_2$ [35]. However, it seems quite rare to find the experimental evidence of such enhanced charge fluctuation at the critical pressure in a Q1D material. This seems to be realized because the electronic CDW transition is decoupled with the structural transition in $Cu_{0.984}Te$ due to the Cu deficiency.

The critical behavior of CDW1 in $Cu_{0.984}Te$ offers new insights into the relation between SC and CDW1. Near P_C, T_C reaches its maximum value of 3.2 K in $Cu_{0.984}Te$. This is much higher than that found in pristine CuTe [12]. The enhancement of T_C near P_C thus suggests that strong CDW1 fluctuation may also contribute to enhance SC, similar to the recent observations in other systems with the CDW-QCP; Ti-doped CsV_3Sb_5 [9], $Lu(Pt_{1-x}Pd_x)_2In$ [38], and 2*H*-$Pd_{0.05}TaSe_2$ [35]. In contrast, CDW2 appears to have minimal effect on SC itself because it emerges above 7.5 GPa. Therefore, our observations here underscore the critical role of CDW1 fluctuation in enhancing superconducting pairing strength in $Cu_{0.984}Te$, possibly through increased electron-electron interaction.

5. Conclusions

We have investigated the pressure-induced evolution of electronic and structural properties in $Cu_{0.984}Te$. Our experimental findings reveal three distinct features that differ from the pristine CuTe. Firstly, CDW1 is completely suppressed near 6 GPa with T_{CDW1} approaching zero, accompanied by enhanced superconductivity with T_C reaching 3.2 K, significantly higher than the 2.3 K observed in the pristine CuTe. Secondly, a pressure-induced structural transition occurs above 6 GPa, where the system transforms from v- CuTe to r- CuTe through an extended coexistence region. Thirdly, CDW2 develops exclusively in the high-pressure r- CuTe phase above 7.5 GPa with T_{CDW2} increasing under pressure up to 11.3 GPa, contrary to its behavior in pristine CuTe. First-principles calculations and Raman spectroscopy suggest that this unique CDW2 phase, resulting in unstable phonon dispersion, is stabilized by the two major effects i.e., large Coulomb interaction and chemical doping effects. These findings show that slight Cu deficiency in CuTe fundamentally modifies structural and electronic phase boundaries, providing new insights into the role of charge density wave order on the stabilization of other electronic orders (i.e., superconductivity and another CDW order) and structural properties in low-dimensional materials.

Supplementary Materials: The following supporting information can be downloaded at: Preprints.org, Figure S1: The scanning electron microscope image of a $Cu_{1-\delta}Te$ single crystal. Table S1: the 5 point average ratio of Cu an Te for 5 pieces of $Cu_{1-\delta}Te$ from the same batch and their averages. Figure S2: The $d\rho/dT$ vs. T plots under pressure. Figure S3: The result of phonon band calculation on the Cu deficient $Cu_{11}Te_{12}$ at 10 GPa with different

 doi:10.20944/preprints202509.2167.v1

Coulomb interaction. Figure S4: The result of phonon band calculation on the pristine CuTe at 10 GPa with different Coulomb interaction. Figure S5: The field derivatives of resistivity at 10 K of a $Cu_{0.984}Te$ single crystal under pressure. Figure S6: the two-band fitting results of the Hall resistivity measured at (a) 3.5 GPa, (b) 6.3 GPa, and (c) 10.1 GPa.

Author contributions: K. –T. K., D. B., and K. H. K. initiated the project. K. –T. K., and D. B. prepared the single crystalline samples. K. –T. K. characterized the samples. K. –T. K. and Y. S. performed the high-pressure transport measurements. I. G and Y. S. performed high-pressure Raman measurements. Z. W., S. K., and D. Y. K. performed the phonon band calculation. K. –T. K. and K. H. K. analysed the data and wrote the manuscript. K. H. K. devised the project and advised the research. All authors discussed the results and commented on the manuscript.

Fundings: K. –T. K., Y. S., I. C., S. K., D. B., and K. H. K. were financially supported by the Ministry of Science and ICT through the National Research Foundation of Korea (2019R1A2C2090648, 2022H1D3A3A01077468), the Ministry of Education (2021R1A6C101B418), and Samsung Electronics Co., Ltd. (0409-20240305). Z. W and D. Y. K. acknowledge the support from National Natural Science Foundation of China (11774015). The authors thank Seolji Kim of the National Center for Inter-university Research Facilities for assistance with the wavelength dispersive x-ray spectroscopy measurements.

Competing Interests: The authors declare no competing interests.

References

1. Bhoi, D.; Khim, S.; Nam, W.; Lee, B. S.; Kim, C.; Jeon, B.-G.; Min, B. H.; Park, S.; Kim, K. H. Interplay of charge density wave and multiband superconductivity in 2*H*-Pd_xTaSe_2, *Sci. Rep.* **6**, 24068 (2016)
2. Kim, C.; Bhoi, D.; Sur, Y.; Jeon, B.-G.; Wulferding, D.; Min, B. H.; Kim, J.; Kim, K. H. Experimental signatures of nodeless multiband superconductivity in a 2*H*-$Pd_{0.08}TaSe_2$ single crystal, *Sci. Rep.* **11**, 13383 (2021)
3. Teng, X.; Chen, L.; Ye, F.; Rosenberg, E.; Liu, Z.; Yin, J.-X.; Jiang, Y.-X.; Oh, J. S.; Hasan, M. Z.; Neubauer, K. J.; Gao, B.; Xie, Y.; Hashimoto, M.; Lu, D.; Jozwiak, C.; Bostwick, A.; Rotenberg, E.; Birgeneau, R. J.; Chu, J.-H.; Yi M.; Dai, P. Discovery of charge density wave in a kagome lattice antiferromagnet, *Nature* **609**, 490 – 495 (2022)
4. Ortiz, B. R.; Teicher, S. M. L.; Hu, Y.; Zuo, J. L.; Sarte, P. M.; Schueller, E. C.; Abeykoon, A. M. M.; Krogstad, M. J.; Rosenkranz, S.; Osbom, R.; Seshadri, R.; Balents, L.; He, J.; Wilson, S. D. CsV_3Sb_5: A Z_2 Topological Kagome Metal with a Superconducting Ground State, *Phys. Rev. Lett.* **125**, 247002 (2020)
5. Nie, L.; Sun, K.; Ma, W.; Song, D.; Zheng, L.; Liang, Z.; Wu, P.; Yu, F.; Li, J.; Shan,M.; Zhao, D.; Li, S.; Kang, B.; Wu, Z.; Zhou, Y.; Liu, K.; Xiang, Z.; Ying, J.; Wang, Z.; Wu T.; Chen, X. Charge-density-wave-driven electronic nematicity in a kagome superconductor, *Nature* **604**, 59 – 64 (2022)
6. Yu, F. H.; Wu, T.; Wang, Z. Y.; Lei, B.; Zhuo, W. Z.; Ying, J. J.; Chen, X. H. Concurrence of anomalous Hall effect and charge density wave in a superconducting topological kagome metal, *Phys. Rev. B* **104**, L041103 (2021)
7. Denner, M. M.; Thomale, R.; Neupert, T. Analysis of Charge Order in the Kagome Metal AV_3Sb_5 (A = K, Rb, Cs), *Phys. Rev. Lett.* **127**, 217601 (2021)
8. Yu, F. H.; Ma, D. H.; Zhuo, W. Z.; Liu, S. Q.; Lei, B.; Ying, J. J.; Chen, X. H. Unusual competition of superconductivity and charge-density-wave state in a compressed topological kagome metal, *Nat. Commun.* **12**, 3645 (2021)
9. Sur, Y.; Kim, K.-T.; Kim, S.; Kim, K. H. Optimized superconductivity in the vicinity of a nematic quantum critical point in the kagome superconductor $Cs(V_{1-x}Ti_x)_3Sb_5$, *Nat. Commun.* **14,** 3899 (2023)
10. Zhang, K.; Liu, X.; Zhang, H.; Deng, K.; Yan, M.; Yao, W.; Zheng, M.; Schwier, E. F.; Shimada, K.; Denlinger, J. D.; Wu, Y.; Duan, W.; Zhou, S. ; Evidence for a Quasi-One-Dimensional Charge Density Wave in CuTe by Angle-Resolved Photoemission Spectroscopy, *Phys. Rev. Lett.* **121**, 206402 (2018)
11. Wang, S.; Chen, X.; An, C.; Zhou, Y.; Zhou, Y.; Gu, C.; Zhang, L.; Yang, X.; Yang, Z. Pressure-induced superconductivity in the quasi-one-dimensional charge density wave material CuTe, *Phys. Rev. B* **103**, 134518 (2021)

 doi:10.20944/preprints202509.2167.v1

12. Wang, S; Wang, Q.; An, C.; Zhou, Y.; Zhou, Y.; Chen, X.; Hao, N.; Yang, Z. Two Distinct Charge Density Wave Orders and Emergent Superconductivity in Pressurized CuTe, *Matter* **6**, 3526-3537 (2023)
13. McWhan, D. B.; Fleming, R. M.; Moncton, D. E.; DiSalvo F. J., Reentrant Lock-in Transition of the Charge Density Wave in 2*H*-$TaSe_2$ at High Pressure, *Phys. Rev. Lett.* **45**, 269-272 (1980)
14. Kresse, G.; Futhmüller, J. Efficiency of ab-initio total energy calculations for metals and semiconductors using a plane-wave basis set. *Comput. Mat. Sci.* **6**, 15-50 (1996)
15. Kresse, G.; Futhmüller, J. Efficient iterative schemes for ab initio total-energy calculations using a plane-wave basis set. *Phys. Rev. B.* **54**, 1169 (1996)
16. Togo, A.; Tanaka, I. First principles phonon calculations in materials science. *Scr. Mater.* **108**, 1-5 (2015)
17. Perdew, J. P.; Burke, K.; Ernzerhof, M. Generalized Gradient Approximation Made Simple. *Phys. Rev. Lett.* **77**, 3865-3868 (1996)
18. Grimme, S.; Antony, J.; Ehrlich, S.; Krieg S. A consistent and accurate ab initio parametrization of density functional dispersion correction (DFT-D) for the 94 elements H-Pu. *J. Chem. Phys.* **132**, 154104 (2010)
19. See Supplemental Material at [url] for further details on the experimental measurements.
20. Barajas-Aguilar, A. H.; Sandoval, S. J. J.; Garay-Tapia, A. M. On the stability of Cu_xTe polytypes: phase transitions, vibrational and electronic properties, *J. Phys.: Condens. Matter* **32** 045403 (2020)
21. Salmón-Gamboa, J. U.; Barajas-Aguilar, A. H.; Ruiz-Ortega, L. I.; Garay-Tapia, A. M.; Sandoval, S. J. J. Vibrational and electrical properties of $Cu_{2-x}Te$ films: experimental data and first principle calculations, *Sci. Rep.* **8**, 8093 (2018)
22. J. L. F. Da Silva, S.-H. Wei, J. Zhou, and X. Wu, Appl. Phys. Lett. **91**, 091902 (2007).
23. Gruner, G. *Density waves in solids* (Frontiers in physics; v. 89. Addison-Wesly Publishing Company, 1994)
24. Kim, S.; Kim, B.; and Kim, K. Role of Coulomb correlations in the charge density wave of CuTe, *Phys. Rev. B*. **100**, 054112 (2019)
25. Feng, Y.; Wang, Y.; Silevitch, D. M.; Yan, J.-Q.; Kobayashi, R.; Hedo, M.; Nakama, T.; Onuki, Y.; Suslov, A. V.; Mihaila, B.; Littlewood, P. B.; Rosenbaum, T. F. Linear magnetoresistance in the low-field limit indensity-wave materials, *Proc. Natl. Acad. Sci. USA* **116**, 11201-11206 (2019)
26. Luo, Y.; Li, H.; Dai, Y. M.; Miao, H.; Shi, Y. G.; Ding D.; Taylor, A. J.; Yarotski D. A.; Prasankumar, R. P.; Thompson, J. D. Hall effect in the extremely large magnetoresistance semimetal WTe_2, *Appl. Phys. Lett.* **107**, 182411 (2015)
27. Vool, U; Hamo, A.; Varnavides, G.; Wang, Y.; Zhou, T. X.; Kumar, N.; Dovzhenko, Y.; Qiu, Z.; Garcia, C. A. C.; Pierce, A. T.; Gooth, J.; Anikeeva, P.; Felser, C.; Narang P.; Yacoby, A. Imaging phonon-mediated hydrodynamic flow in WTe_2, *Nat. Phys.* **17**, 1216 – 1220 (2021)
28. Jaramillo, R.; Feng, Y.; Wang, J.; Rosenbaum, T. F. Signatures of quantum criticality in pure Cr at high pressure, *Proc. Natl. Acad. Sci. USA* **107**, 13631-13635 (2010)
29. Zhang, K.; Cao, Z.-Y.; Chen, X.-J. Appl. Phys. Lett. **114**, 141901 (2019).
30. Monceau, P. Electronic crystals: an experimental overview, *Adv. Phys*. **61**, 325 (2012)
31. Freitas, D. C.; Rodière, P.; Núñez, M.; Garbarino, G. Sulpice, A.; Marcus, J.; Gay, F.; Continentino, M. A.; Núñez--Regueiro, M. Phys. Rev. B **92**, 205123 (2015).
32. Núñez--Regueiro, M.; Mignot, J.-M.; Castello, D. Europhys. Lett. **18**, 53 (1992).
33. Yamaguchi, T.; Ueda, Y. Phys. Rev. B **77**, 104529 (2008).
34. Monteverde, M.; Lorenzana, J.; P. Monceau, P.; Núñez--Regueiro, M. , Phys. Rev. B **88**, 180504 (2013).
35. Sur, Y.; Gim, D.-H.; Bhoi, D.; Jang, D.H.; Murata, K.; Hu, J.-W.; Zhang, K.; Cao, Z.; Struzhkin, V.; Chen, X.-J.; Kim, K.H. Enhanced superconductivity near a pressureinduced quantum critical point of strongly coupled charge density wave order in 2*H*-$Pd_{0.05}TaSe_2$ NPG Asia Mater. **17**, 8 (2025)
36. Kadowaki, K.; Woods, S. Universal relationship of the resistivity and specific heat in heavy-fermion compounds. Solid State Commun. **58**, 507-509. (1986)
37. Marder, M. Condensed Matter Physics, 2nd ed.; John Wiley & Sons: Hoboken, NJ, USA, 2010.
38. Gruner, T.; Jang, D.; Huesges, Z.; Cardoso-Gil, R.; Fecher, G. H.; Koza, M. M.; Stockert, O.; Mackenzie, A. P.; Brando, M.; Geibel, C. Charge density wave quantum critical point with strong enhancement of superconductivity, *Nat. Phys.* **13**, 967-972 (2017)

 doi:10.20944/preprints202509.2167.v1

39. Li, X.; Huang, X.; Wang, X.; Liu, M.; Wu, G.; Huang, Y.; He, X.; Li, F.; Zhou, Q.; Liu, B.; Cui, T. High-pressure dissociation of selenium and tellurium. Phys. Chem. Chem. Phys. **20**, 6116–6120. (2018)
40. Pine, A. S.; Dresselhaus, G. Raman Spectra and Lattice Dynamics of Tellurium. Phys. Rev. B 1971, 4(2), 356–371.